Study of Rain Events over the South China Sea by Synergistic Use of Multi-sensor Satellite and Ground-based Meteorological Data

Werner Alpers, Cho Ming Cheng, Yun Shao, and Limin Yang

Abstract

Rain cells and rain bands over the South China Sea off the coast of Hong Kong are studied by using multi-sensor satellite and ground-based meteorological data. These include synthetic aperture radar (SAR) images acquired by the Advanced Synthetic Aperture Radar (ASAR) onboard the European ENVISAT satellite, weather radar images from the Hong Kong Observatory (HKO), rain rate data acquired by the Special Sensor Microwave Imager (SSM/I) sensor onboard the F15 satellite of the American Defense Meteorological Satellite Program (DMSP) and the rain sensors onboard the Tropical Rainfall Measurement Mission (TRMM) satellite, cloud image of GOES-9 satellite, sea surface wind maps acquired by the scatterometer onboard the QUIKSCAT satellite, and meteorological data from weather stations in Hong Kong. Three rain events, typical of Hong Kong, are studied. The first event consists of a cluster of rain cells associated with the summer monsoon, the second one of rain cells aligned in a rain band generated by an upper-air trough, and the third one consists of small rain cells embedded in a cold front. It is shown that ASAR images, which have a resolution of 30 m in the Image Mode (IM) and 150 m resolution in the Wide Swath Mode (WSM), yield much more detailed information on the spatial structure of rain events over the ocean than data obtained from SSM/I and the rain sensors onboard the TRMM satellite. The precipitation radar (PR) onboard TRMM, which is the rain measuring instrument flown in space with the next best resolution, has a resolution of only 4 km. However, the disadvantage of SAR is that it is sometimes difficult to identify SAR signatures visible on SAR images of the sea surface unambiguously as caused by rain events. By comparing SAR images with simultaneously acquired weather radar images of the Hong Kong Observatory, a better knowledge of radar signatures on SAR images resulting from rain events over the ocean is obtained. This knowledge then helps greatly in detecting rain events on SAR images which are acquired over ocean areas, which are not in the reach of weather radar stations. SAR *images containing radar signature of rain events allow a much more detailed study of fine-scale structures of rain events over the World's ocean, in particular of clusters of rain cells, than any other sensor presently flown in space.*

Introduction

Conventionally, rain events are studied by means of ground-based observations using automatic weather station readings and weather radar images. Weather radars detect the location and intensity of rain events by emitting microwave pulses from a rotating antenna and detecting the returned pulses as a function of time by range gating (Sauvageot, 1992). Thus, images of the spatial distribution of backscattered radar power or radar reflectivity due to microwave backscattering (and attenuation) by raindrops in the atmosphere are obtained. By using an empirical relationship between backscattered radar power and rain rate, these images are converted into rain rate maps. The weather radar of the Hong Kong Observatory (HKO), which operates at 2.82 GHz (S-band), is a Doppler weather radar capable of measuring not only the backscattered radar power, but also the velocity of the rain drops along the viewing direction of the antenna (Doppler velocity or radial velocity).

With the advent of satellite technology, rain-bearing weather systems can also be measured from space. Spaceborne instruments capable of yielding information on rainfall include the Special Sensor Microwave Imager (SSM/I) sensor onboard satellites of the American Defense Meteorological Satellite Program (DMSP), the microwave instrument (TMI) and the precipitation radar (PR) flying onboard the U.S.-Japanese Tropical Rainfall Measuring Mission (TRMM) satellite (Simpson *et al.*, 1996; Kummerow *et al.*, 1998). All these spaceborne instruments have relatively coarse spatial resolution (the best is the precipitation radar onboard the TRMM satellite with a resolution of 4 km) and thus cannot resolve individual rain cells which often have an extent of only a few kilometers or even less. The microwave radiometers SSM/I and TMI extract rain information from the intensity

Werner Alpers is with the Centre for Marine and Climate Research, Institute of Oceanography, University of Hamburg, Hamburg, Germany (alpers@ifm.uni-hamburg.de).

Cho Ming Cheng is with the Hong Kong Observatory, Hong Kong.

Yun Shao and Limin Yang are with the Joint Laboratory for Geoinformation Science, The Chinese Academy of Sciences and Chinese University of Hong Kong, Hong Kong.

Photogrammetric Engineering & Remote Sensing
Vol. 73, No. 3, March 2007, pp. 267–278.

0099-1112/07/7303–0267/$3.00/0

of microwave radiation emitted by rain drops in the atmosphere, whereas the Precipitation Radar obtains the rain information from both the scattering and the attenuation of the radar pulses by rain drops in the atmosphere.

Since the time of the SEASAT satellite mission in 1978, it has been noticed that footprints of rain cells can be detected on SAR images of the sea surface (Fu and Holt, 1982; Atlas, 1994a; Jameson *et al.*, 1997; Moore *et al.*, 1997; Melsheimer *et al.*, 1998 and 2001). These observations have opened up the possibility of studying the distribution of rain cells over the ocean with high horizontal resolution (10 to 100 m) on a global scale. However, it is still a research issue as to how to extract quantitative information on rain rates from these radar images.

Rain cells over the ocean become visible on SAR images because (a) they cause changes of the sea surface roughness and thus changes of the microwave backscattered power (surface scattering), and (b) the microwaves are scattered and attenuated by the raindrops (or hydrometeors) in the atmosphere (volume scattering and attenuation). For SARs operating at long wavelengths, e.g., the L-band SAR onboard the SEASAT satellite (wavelength: 23 cm), the radar signatures of rain cells originate almost exclusively from surface scattering, while for SARs operating at shorter wavelengths they originate from both, i.e., from surface scattering as well as from volume scattering and attenuation by rain drops in the atmosphere (for a detailed discussion see Melsheimer *et al.*, 1998, and Alpers and Melsheimer, 2004). For the C-band SARs onboard the European satellites ERS-1, ERS-2 and ENVISAT and the Canadian RADARSAT satellite, which all operate at a radar wavelength of 5.6 cm, the radar signatures of rain cells are usually dominated by surface scattering. But for very heavy rainfall, attenuation of the radar signals by raindrops in the atmosphere can be dominant (Lin *et al.*, 2001).

The radar backscattering from the rough sea surface at incidence angles (incidence angle = angle between nadir and the radar beam) between 20° and 70° can be described by Bragg scattering theory (Valenzuela, 1978). The power of the backscattered radar signal is proportional to the amplitude squared of those water waves which propagate towards or away from the look direction of the radar antenna and which have wavelength of $\lambda_B = \lambda_0/2\sin\theta$, where λ_0 denotes the radar wavelength and θ denotes the incidence angle of the radar beam. The wavelength λ_B is called Bragg wavelength. The Bragg wavelengths for the SAR onboard the ENVISAT satellite, called Advanced Synthetic Aperture Radar (ASAR), whose frequency is 5.33 GHz corresponding to a wavelength of 5.6 cm, vary between 4 cm and 9 cm depending on incidence angle.

The amplitude of the Bragg waves is modified by rain by two effects, which change the sea surface roughness: (a) by winds (downdraft and updraft) associated with the rain cells, and (b) by raindrops impinging onto the sea surface.

Downdraft winds are often very strong and give rise to a strong increase of the sea surface roughness, while updraft winds are less strong. Downdrafts spread on the sea surface usually in radial direction and are visible on SAR images as bright patterns surrounding the rain cell centres and having sharp outer boundaries. If there is no ambient wind, then the radar signature of the outer boundary of the downdraft often has a circular shape, while in the presence of an ambient wind it has an elliptical shape.

Raindrops impinging onto the sea surface generate ring waves which enhance the sea surface roughness (Tsimplis, 1992; Bliven *et al.*, 1997; Craeye *et al.*, 1997), but they also generate turbulence in the upper water layer which decreases the sea surface roughness because turbulence attenuates the small-scale waves and thus the Bragg waves (Nystuen, 1990). Both effects compete with each other, and it depends primarily on the wavelength of the water waves to determine which one is dominant. But generation and attenuation of the Bragg waves depends also on rain rate, drop size distribution, wind speed, and temporal evolution of the rain event. At the initial stage of the rain event, the turbulence in the upper water layer is not fully developed, and thus, its damping effect on the water waves is small. After it has stopped raining, the turbulence does not decay immediately (the life time of the turbulence is of the order of a minute) and continues to attenuate the waves even after the rainfall has stopped. For the C-band Bragg waves (responsible for the radar backscattering of the ERS, ENVISAT, and RADARSAT SAR signals from the sea surface), the amplitude of the Bragg waves is most often reduced in areas where raindrops impinge onto the sea surface and less often enhanced. Thus rain cells become visible on C-band SAR images usually as patches consisting of irregular dark areas in the center surrounded by a broad bright rim arising from the downdraft. But sometimes the centers consist also of a mixture of dark and bright areas.

In the following, we present three case studies of rain events visible on SAR images, which were acquired by the European ENVISAT satellite over the South China Sea off the coast of Hong Kong, and compare them with quasi-simultaneously acquired data from other sensors.

Case Studies

The three ENVISAT ASAR images used in our case studies were all acquired during descending satellite paths (flight direction from north to south) over the South China Sea near Hong Kong around 0222 UTC or 1022 Hong Kong Time (HKT). Since the radar antenna looks to the right of the satellite track, the image intensity in the right hand section of the SAR image is brighter than in the left hand section. This is due to the fact that (a) the sea surface is viewed by the SAR under an incidence angle that increases from the right-hand side of the image (near range) to the left hand side (far range), and that (b) the radar backscattering from the sea surface decreases with increasing incidence angle.

We compare the three ENVISAT ASAR images presented in this paper with quasi-simultaneously acquired weather radar images from the Hong Kong Observatory (HKO) and, when available, also with other quasi-simultaneously acquired satellite data and with in-situ measured meteorological data. These three examples comprise three different kinds of rain events: (a) a cluster of rain cells associated with the summer monsoon, (b) rain cells aligned in a rain band associated with an upper-air trough, and (c) small rain cells embedded in a cold front.

The 05 August 2004 Rain Event

The rain event of 05 August 2004 is a typical event in Hong Kong in the summer monsoon season. The ENVISAT ASAR image depicted in Figure 1b, which was acquired on 05 August 2004 at 0222 UTC, consists of a cluster of convective rain cells of different sizes (and durations). The radar signatures of most of these rain cells have the "classical" doughnut-type shape with a black center surrounded by a bright area caused by downdraft, which was described previously in several papers (Atlas, 1994a and 1994b; Melsheimer *et al.*, 1998 and 2001; Alpers and Melsheimer, 2004). The radar signatures of rain cells visible on the ASAR image have their correspondence in the weather radar image depicted in Figure 1a, which was acquired at 0224 UTC or 1024 Hong Kong Time (HKT). The weather radar image is a 3 km Constant Height Plan Position Indicator (CAPPI) image which displays the rain rate at a height of 3 km. The ENVISAT ASAR image shows approximately at the same location very distinct surface patterns which we interpret as sea surface manifestations of rain cells. For three distinct rain cells, this

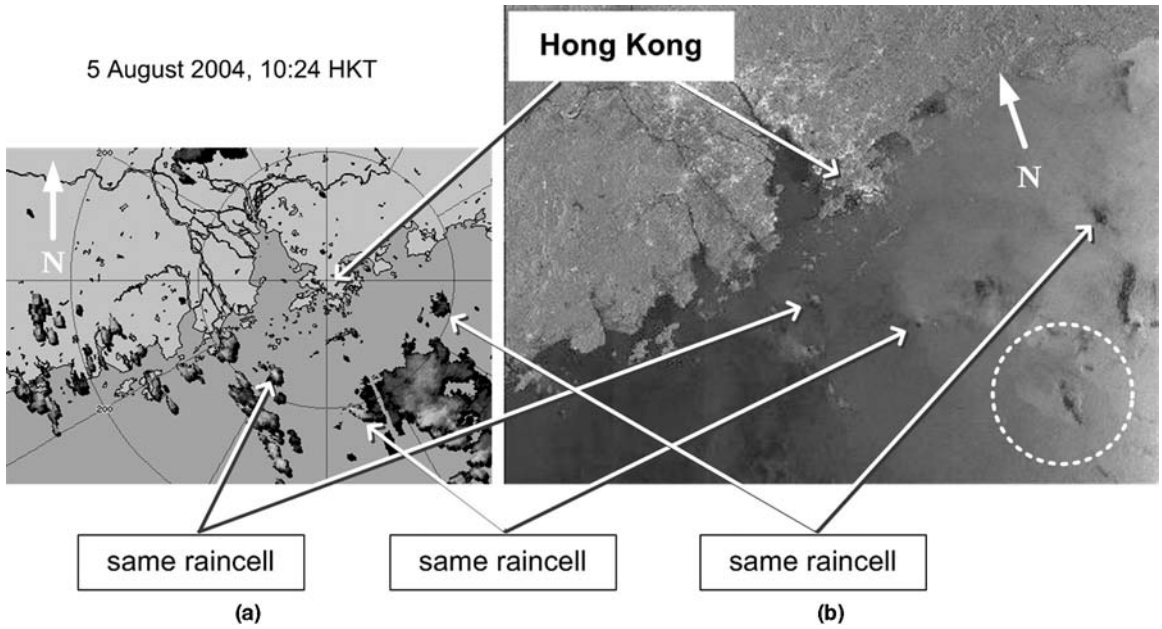

Figure 1. ENVISAT ASAR image (b; ©ESA) acquired in the wide swath mode on 05 August 2004 at 0222 UTC (1022 HKT) and the corresponding weather radar image (3 km CAPPI image) (a; ©HKO) of the Hong Kong weather radar acquired at 0224 UTC. The range circles in the weather radar image are 100 km apart. Rain rate is represented in grey shades (increasing from dark grey to light grey). The image area of the ENVISAT SAR image is 380 km × 400 km. The white dashed circle in the ASAR image denotes the feature shown in Figure 2.

correspondence is marked by three arrow pairs. Note that the correspondence cannot be exact since the SAR measures the rain signature at the sea surface, while the weather radar measures the rain signature in the atmosphere, in this case (Figure 1a) at a height of 3 km. The raindrops which are detected at a given time in the atmosphere by the weather radar are not the same as those which modify the sea surface roughness at the same time and are detected by the SAR, because it takes some time for the rain drops to fall to the sea surface. Taking a typical terminal fall speed of raindrops of around 6.5 ms^{-1}, it would take the raindrops about eight minutes to reach the sea surface from a height of 3 km, provided that there is no lateral drift. Figure 2 shows an enlargement of the lower right-hand section of the ASAR image depicted in Figure 1 containing a typical radar signature of a rain cell: black patches surrounded by a broad bright area. We interpret the dark patches as areas where the raindrops hit the sea surface and cause a damping of the Bragg waves and the surrounding bright area as the area where the downdraft wind roughens the sea surface.

The distribution of the rain cells was measured quasi-simultaneously by the SSM/I onboard the F15 satellite of the DMSP satellite series and by the rain sensors onboard the TRMM satellite. The rain rate map derived from SSM/I data acquired on 05 August 2004 at 0206 UTC is depicted in Figure 3 and the accumulated rainfall derived from TRMM data (level 3 TRMM product 3B42 = TRMM; Adjusted Merged-Infrared Precipitation) acquired on 05 August between 0000 UTC and 0300 UTC is depicted in Figure 4. By comparing these two maps with the ASAR image, it can be seen that the ASAR image reveals much finer-scale structures of the rain event than the SSM/I and the TRMM maps.

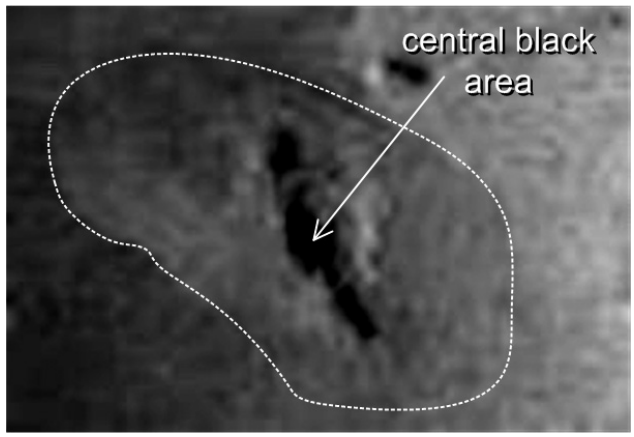

Figure 2. Enlargement of the lower right-hand section of the ASAR image depicted in Figure 1 showing a typical radar signature of a rain cell. The center is often black which (in the case of not too heavy rain) is believed to result from damping of the Bragg waves by turbulence generated in the upper water layer by the impinging raindrops. The wide bright area (enclosed in dotted region) surrounding the black area results from roughening of the sea surface by downdraft winds associated with the rain cell.

The 08 May 2004 Rain Event

The rain event of 08 May 2004 was triggered by an upper-air trough resulting in an organized rain band with multiple embedded rain cells. The ENVISAT ASAR image depicted in Figure 5, which was acquired in the wide swath mode on 08 May 2004 at 0222 UTC (1022 HKT), shows the sea surface manifestations of this rain band. It appears as a zigzag bright band stretching from the northeast to the southwest with increasing width towards the northeast. Small dark spots

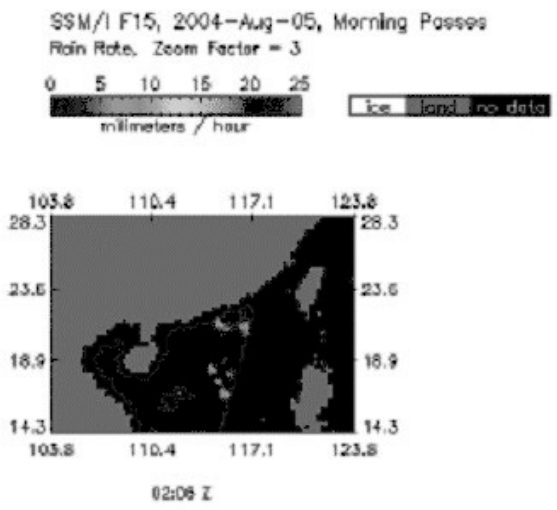

Figure 3. Distribution of rain rate measured by SMM/I on 05 August 2004 at 0206 UTC. The grey scale on the top denotes rain rate in mm/h. The rain cells are poorly resolved (grey patches over the sea).

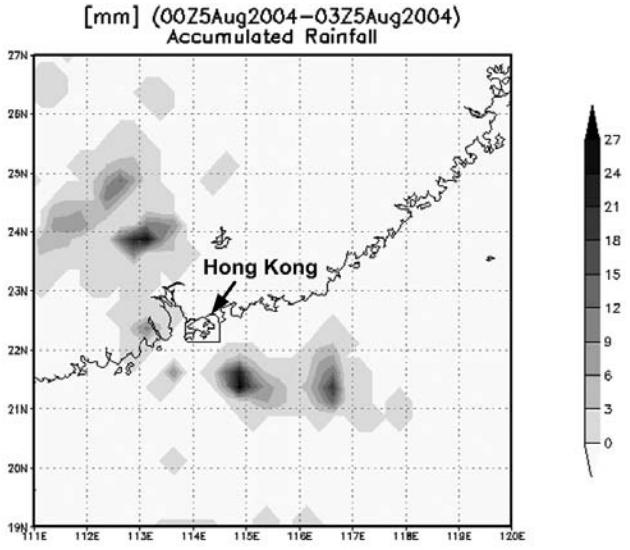

Figure 4. Distribution of accumulated rainfall measured by the TRMM satellite on 05 August 2005 between 0000 UTC and 0300 UTC. The grey scale on the right denotes accumulated rainfall in mm. In this plot the rain cells are much better resolved spatially than in the plot generated from SSM/I data depicted in Figure 3. Also the rain rate is better resolved.

embedding in the bright band are also evident. The rain rate map retrieved from data of the TRMM satellite acquired between 0000 UTC and 0300 UTC, which is shown in Figure 6, illustrates also a rain band off the coast of Hong Kong.

The weather radar image at 0224 UTC (1024 HKT) depicted in Figure 7 shows approximately at the same location a rain band containing multiple rain cells with high rain rates. When comparing the widths of the bands in both

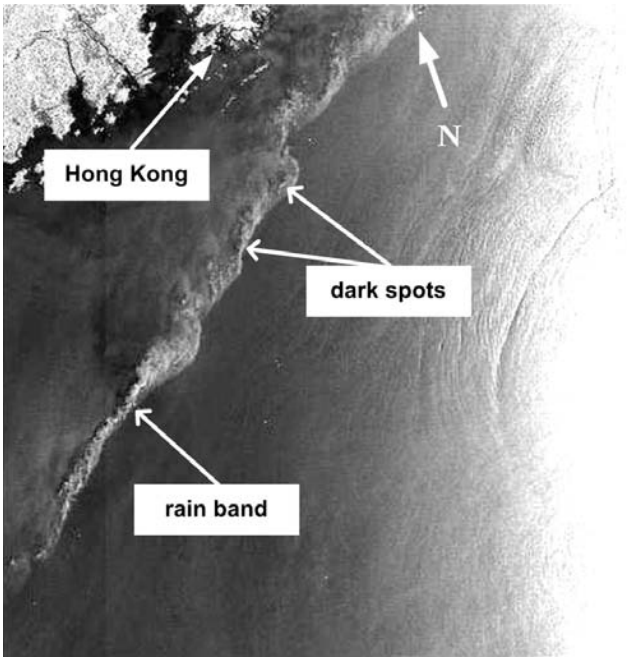

Figure 5. ENVISAT ASAR image acquired in the wide swath mode on 08 May 2004 at 0222 UTC showing sea surface manifestations of a rain band stretching along the coast near Hong Kong. The radar signature of this rain band is quite complex. The bright areas/lines at the southeastern boundary of the rain band (front) are very likely caused by strong downdraft winds. The higher image brightness on the right hand side of the image results from the lower incidence angle at which the sea surface was viewed by the SAR in this section. Sea surface manifestations of internal solitary waves (curved "ripples") are also visible in this section. Image area is 380 km × 400 km (©ESA).

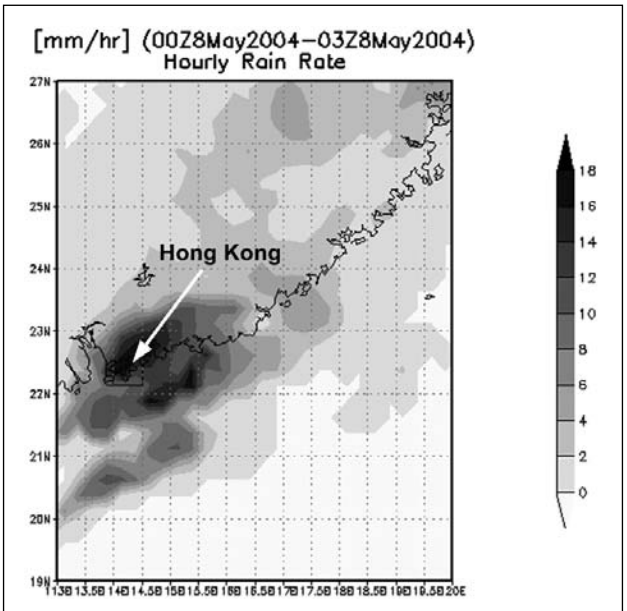

Figure 6. Distribution of rain rate measured by the TRMM satellite on 08 May 2004 between 0000 UTC and 0300 UTC. The grey scale on the right denotes the hourly rain rate in mm/h.

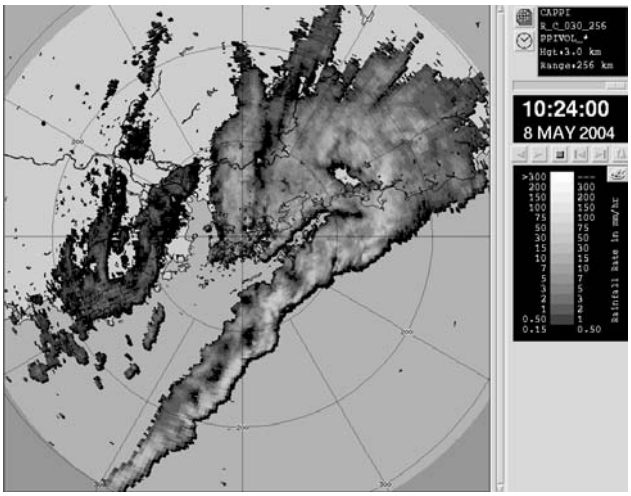

Figure 7. Weather radar image (3 km CAPPI image) acquired by the Hong Kong weather radar on 08 May 2004 at 0224 UTC showing a rain band lying close to the coast. Rain rates are represented in grey shades (increasing from dark grey to light grey) (©HKO).

images, we note that only the areas with high rain rates give rise to a radar signature in the ASAR image. Since the rain band in the ASAR image is, in most parts, visible as a band of increased radar backscattering (compared to the background), we conclude that it is caused primarily by roughening of the sea surface by strong downdraft winds.

An infrared cloud image acquired by the GOES-9 satellite on 08 May 2004 at 0223 UTC is depicted in Figure 8. It shows a bright band of clouds with deep convection extending from the eastern part of China to the sea area southwest of Hong Kong where it took on a wedge-like shape. The northern edge of this cloud band over the South China Sea coincides well with the northern edge of the rain band visible in the weather radar image depicted in Figure 7. It is noted that only the northern portion of the cloud band is rain-bearing.

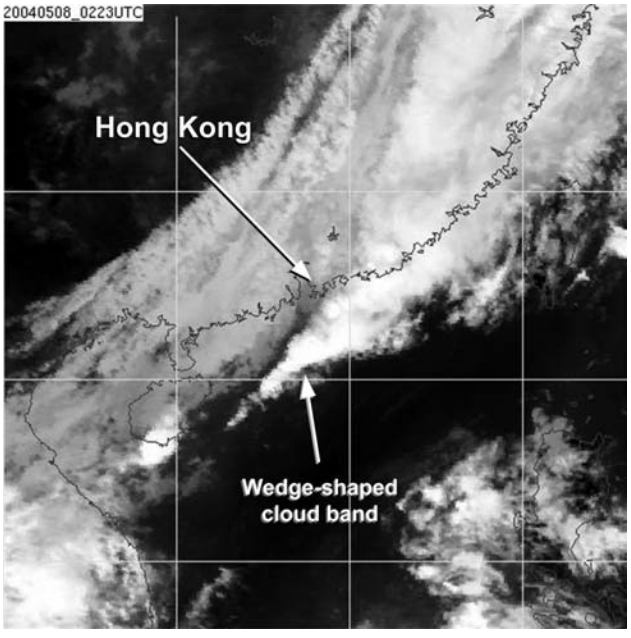

Figure 8. Infrared satellite image from GOES-9 geostationary meteorological satellite acquired on 08 May 2004 at 0223 UTC showing a wedge-like convective cloud band to the southwest of Hong Kong.

From the time sequence of weather radar images, we can infer the direction and speed of the movement of the rain band. Two such images are depicted in Figure 9: the first one was acquired at 0100 UTC (0900 HKT) and the second one at 0324 UTC (1124 HKT). We see that the rain band was moving in a southeasterly direction, and that its speed was around 25 km h^{-1}. Furthermore, this sequence of the weather radar images shows that the width of the rain band widened while propagating southeastward over the sea.

By comparing weather radar images which were acquired at short time separation, we are able to track the motion of individual rain cells within the rain band. Two images acquired at 0200 UTC (1000 HKT) and 0224 UTC (1024 HKT) are depicted in Plate 1a. We see that within the rain band the

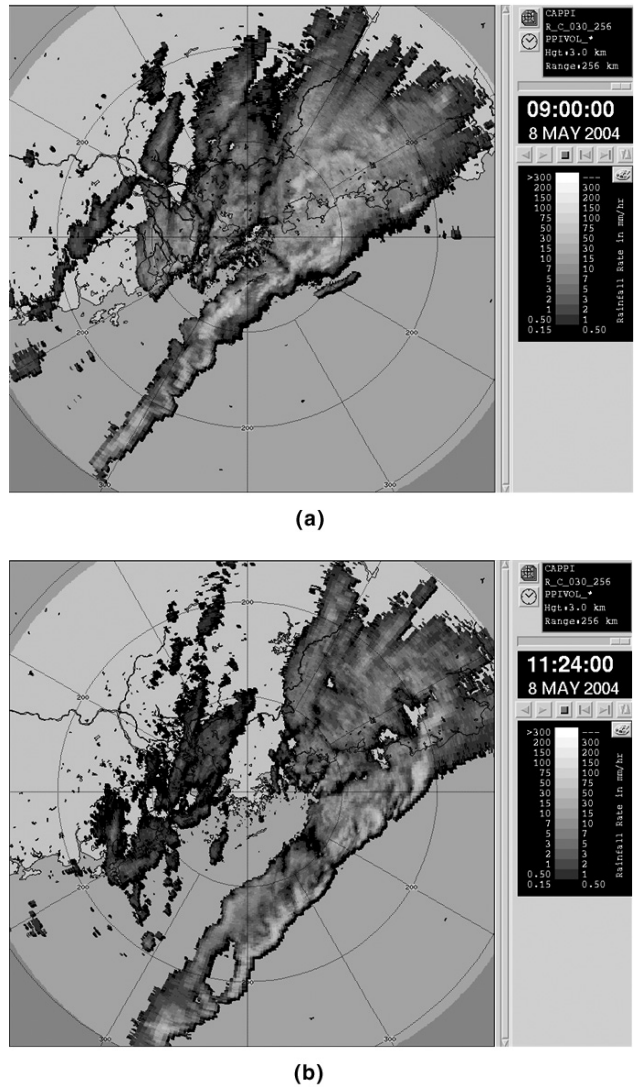

Figure 9. Weather radar images (3 km CAPPI images) acquired by the Hong Kong weather radar on 08 May 2004 at 0100 UTC (a) and at 0324 UTC (b) showing the movement of the rain band in a southeasterly direction (©HKO).

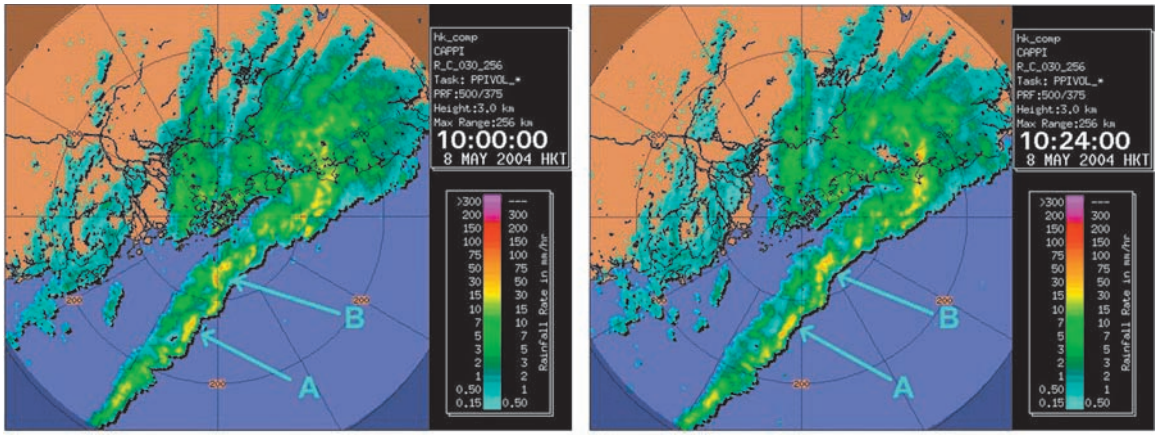

(a)

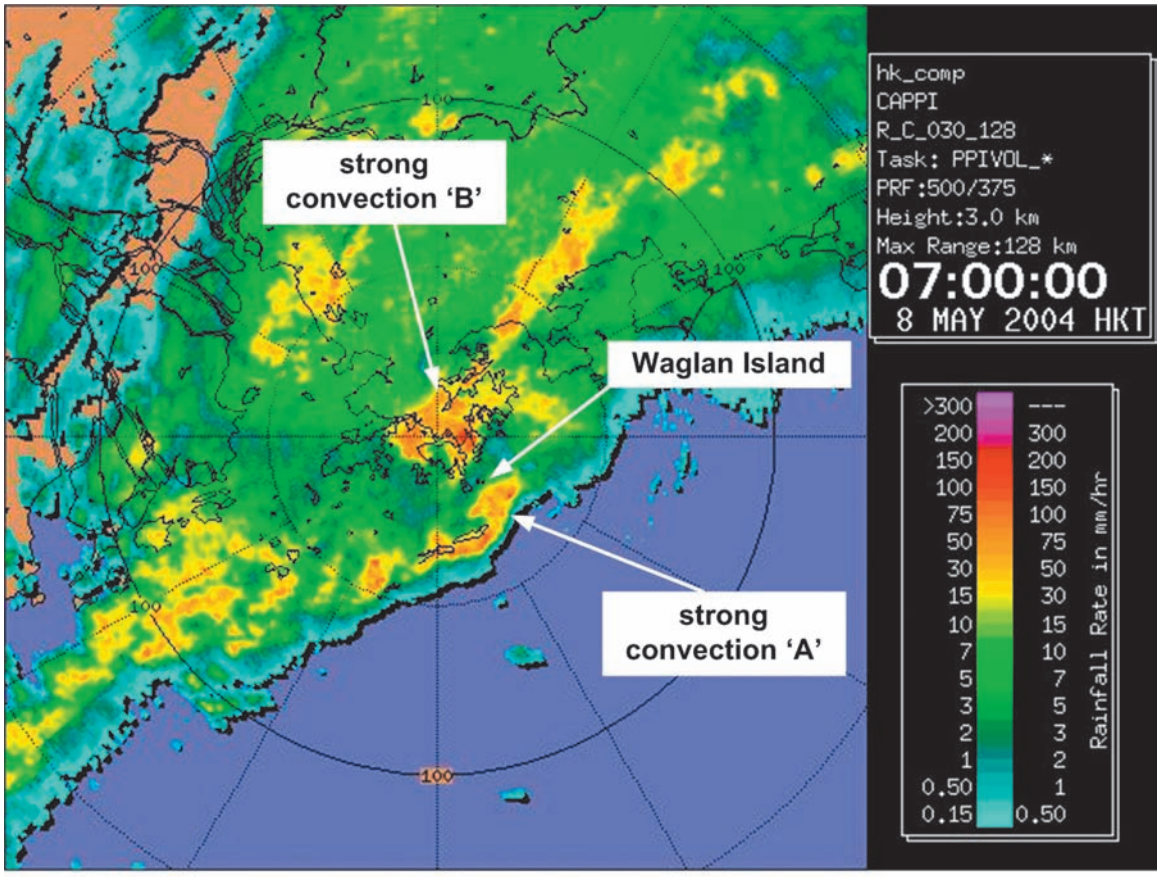

(b)

Plate 1. Weather radar images (3 km CAPPI images) acquired by the Hong Kong weather radar on: (a) 08 May 2004 at 0200 UTC (left) and at 0224 UTC (right) showing the motion of rain cells (marked in "A" and "B") within the rain band in a northeasterly direction. (b) 07 May 2004 at 2300 UTC (08 May 2005 at 0700 HKT) showing areas of strong convection (marked as "A" and "B") near Waglan Island. The colors denote rain rates (increasing from blue to red) (©HKO).

areas with higher rain rates (marked in "A" and "B" in Plate 1a) move on the average in a northeasterly direction.

The Hong Kong weather radar can also measure the component of the velocity of the raindrops in viewing direction of the antenna, also called the Doppler velocity. In Figure 10 the Doppler velocity measured at 0224 UTC (1024 HKT) is depicted. The black arrow inserted in Figure 10 points from the dark grey region (velocity towards the antenna) to the light grey region (velocity away from the antenna) and lies perpendicular to the *white* line known as the region of zero isodop (i.e., region with zero Doppler shift). The arrow indicates that the raindrops move within

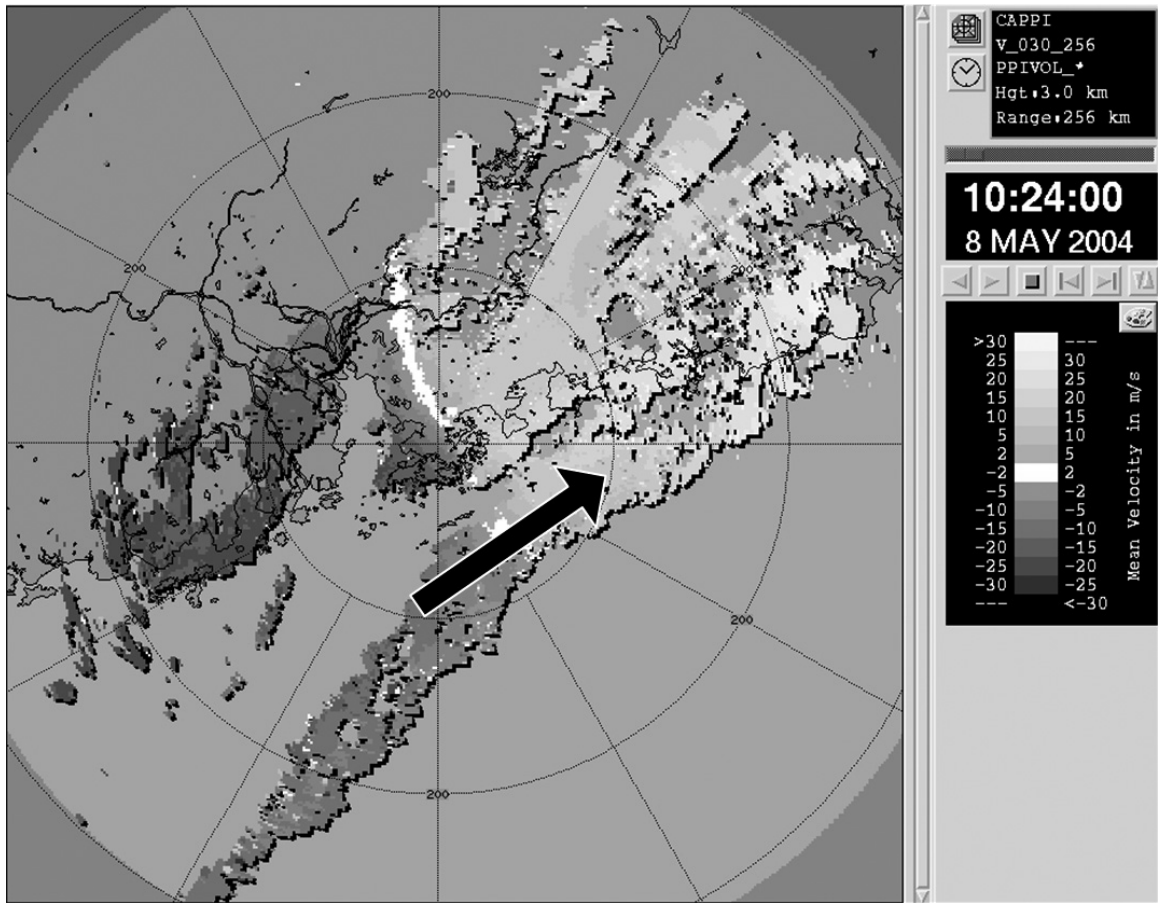

Figure 10. Weather radar image (3 km CAPPI image) of Doppler velocity from the Hong Kong weather radar on 08 May 2004 at 0224 UTC. Positive velocities (in light grey shades) are defined as velocities away from the antenna. The black arrow denotes the direction of movement of the rain drops (©HKO).

the rain band in a northeasterly direction. This direction of motion is consistent with the direction of motion of the rain cells observed in the sequence of weather radar images depicted in Plate 1a.

Weather observations carried out on 08 May 2004 show the following: in the morning of 08 May 2004, a rainstorm associated with the rain band affected the coast of southern China, bringing heavy rainfall and widespread thunderstorms to the region. The rainstorm brought more than 100 mm of rain to Hong Kong in just a few hours in the early morning hours. The rainstorm was associated with an upper-air trough. The wind charts at the 850 hPa level (about 1.5 km above sea level) and at the 200 hPa level (about 12 km above sea level) of 08 May 2004 at 0000 UTC are depicted in Plate 2a and 2b, respectively. The 850 hPa level wind chart in Plate 2a shows a deep trough (the line in yellow colour) lying across southern China. Along and on the eastern side the trough, there was positive vorticity of winds (i.e., rotation of winds in anti-clockwise direction). Near Hong Kong, the value of vorticity was 3.9×10^{-5} s^{-1} (in green color). This trough had a coherent vertical structure all the way to the 200 hPa level, see Plate 2a. The wind chart at the 200 hPa level shows on 08 May 2004 at 0000 UTC, a region of strong divergence of winds (in red color) on the eastern flank of the trough (the line in dark green color). The value of the wind divergence above Hong Kong was high at 5.6×10^{-5} s^{-1} (in yellow to red colors). The radiosonde data of Hong Kong on 08 May 2004 at 0000 UTC (not reproduced here) also show a moist and unstable atmosphere with a high K-index of 37. These atmospheric conditions favoured the development of convective activity. We conjecture that the coherent structure of the upper-air trough, together with the low-level positive vorticity and upper-air strong divergence, resulted in the formation of the narrow rain band visible in the ASAR and weather radar images depicted in Figure 5 and Figure 7, respectively.

In addition to heavy rain, the rain band was also associated with abrupt wind changes. Figure 11 shows the 1-minute mean wind and 1-minute mean sea level pressure at Waglan Island during the passage of the rainstorm. Waglan Island is located in the southeastern part of Hong Kong, about 5 km off the main territory, and has good exposure to winds.

It can be seen from these weather station readings that the winds started off from the southeast at about 7.5 ms^{-1}. Thereafter, the 1-minute mean wind speed plot (Figure 11, thick line) exhibits a double-peak. The first peak in wind speed at 26 ms^{-1} is associated with a sudden drop in atmospheric pressure from the *pre-storm* level of 1005 hPa to a low of 1001 hPa, a drop of 4 hPa within an hour. This signalizes the approach of a low pressure trough. The second peak with wind speed at 23.6 ms^{-1} occurred when

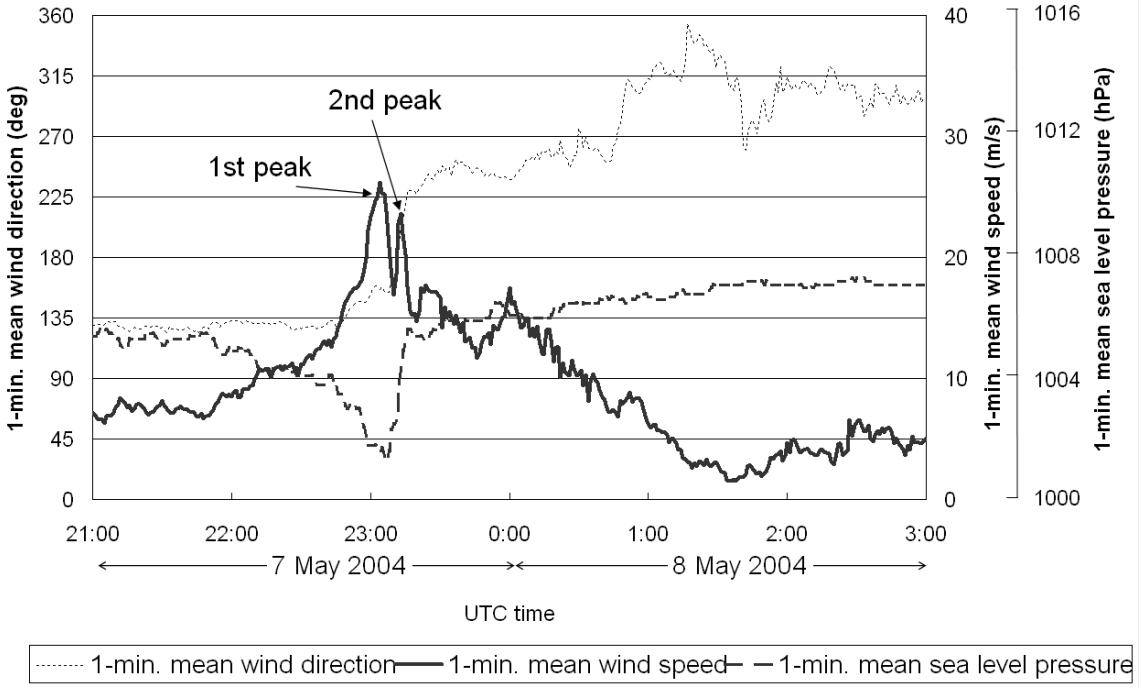

Figure 11. Time series of wind direction, wind speed and mean sea level pressure recorded at Waglan Island, Hong Kong, during the passage of the rainstorm on 07 and 08 May 2004. The sudden increase in wind speed, change in wind direction, and drop of air pressure around 2300 UTC on 07 May 2004 are interpreted as being caused by strong downdraft winds associated with the passage of a strong convective rain area (see Plate 1b).

the winds shifted abruptly from the southeast to the southwest. Thereafter, the winds stayed from the southwest for around one and a half hour before veering further to the northwest.

We interpret the sudden increases in wind speed on 07 May 2004 at 2300 UTC as being caused by strong downdraft associated with a strong convective rain cell. Indeed, the weather radar image acquired on 07 May at 0700 UTC, which is depicted in Plate 1b, shows a large convective rain cell (marked as "A") with rain rate exceeding 50 mm/h to the southeast of Waglan Island. We conjecture that this convective rain cell "A" caused the strong southeasterly winds at Waglan Island (the first peak in wind speed in Figure 11). Plate 1b also shows another larger patch of rain area (marked as "B") with rain rate exceeding 50 mm/h to the northwest of Waglan Island. This rain area subsequently moved east to northeast just to the north of Waglan Island causing the second peak in wind speed.

The 02 March 2004 Rain Event

The rain event of 02 March 2004 was associated with a cold front propagating over the South China Sea in a southerly direction. The ENVISAT ASAR image depicted in Figure 12, which was acquired in the image mode (swath type I2, VV polarization) on 02 March 2004 at 0225 UTC (1025 HKT), shows distinctively a bright area of high sea surface roughness (high wind speed) over the sea to the south of Hong Kong and a dark area of lower sea surface roughness (low wind speed) further south. In the southern dark area, the wind speed must have been partly below the threshold for Bragg wave generation, which is about 2 ms^{-1}, such that no waves were present to backscatter the microwaves from ASAR. The boundary between the bright and dark areas is a wind front. In the ASAR image, embedded in the wind front, are small dark patches, which we interpret as areas where the sea surface roughness decreased due to the damping of the Bragg waves caused by the impinging rain drops onto the sea surface. An enlargement of the frontal area in which the sea surface manifestations of the small rain cells can be seen in greater detail is depicted in Figure 13.

A weather radar image, which was acquired on 02 March at 0224 UTC (1024 HKT), is depicted in Figure 14. It shows small-scale rain cells aligning along a line. When comparing the ASAR image with this weather radar image, we note that the locations of the rain cells in the weather radar image closely correspond to the locations of the dark patches in the ASAR image. This confirms our previous supposition that the black spots in the ASAR image are sea surface manifestations of small rain cells.

The frontal line on the ASAR image is in fact a cold front, as seen on the surface weather map of 02 March 2004 at 0000 UTC (0800 HKT) depicted in Figure 15. This front is an east-west oriented cold front which moved southward across southern China and passed through Hong Kong on 01 March 2004. On 02 March 2004 at 0000 UTC the cold front had moved to the northern part of the South China Sea about 200 km south of Hong Kong. The cold front did not carry much precipitation, making it barely visible on the weather radar image (Figure 14).

The atmospheric front is also identifiable on the sea surface wind field map generated from QUIKSCAT data acquired on 01 March 2004 around 2124 UTC see Figure 16.

Figure 12. ENVISAT ASAR image acquired in the image mode on 02 March 2004 at 0225 UTC showing sea surface manifestations of a cold front with embedded small rain cells (elongated dark patches in the bright area near the frontal line at the center of the image). The bright area in the upper section of the image is a high wind speed area (wind speed around 15 ms^{-1}) and the dark area in the lower section is a low wind speed area (wind speed around 2 to 5 ms^{-1}). Imaged area is 280 km $\times$ 100 km (©ESA).

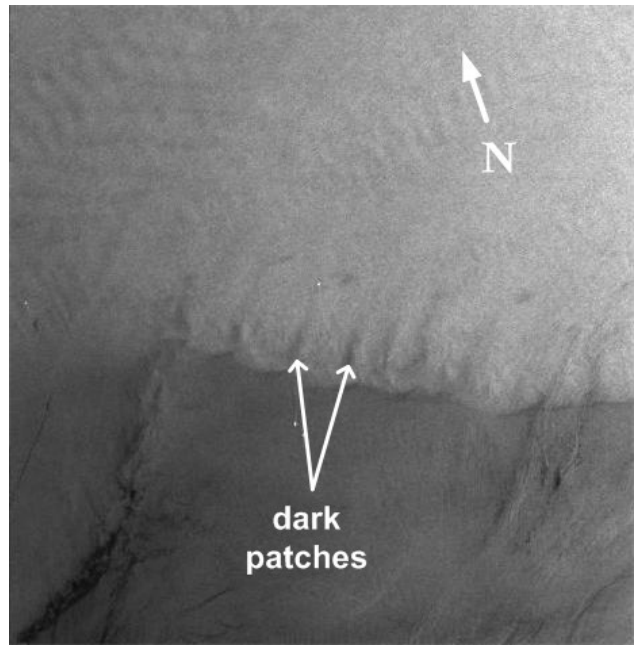

Figure 13. Enlargement of the frontal feature visible in the ASAR image depicted in Figure 12 showing radar signatures of small rain cells (dark elongated patches accompanied by patches with slightly increased image intensity) (©ESA).

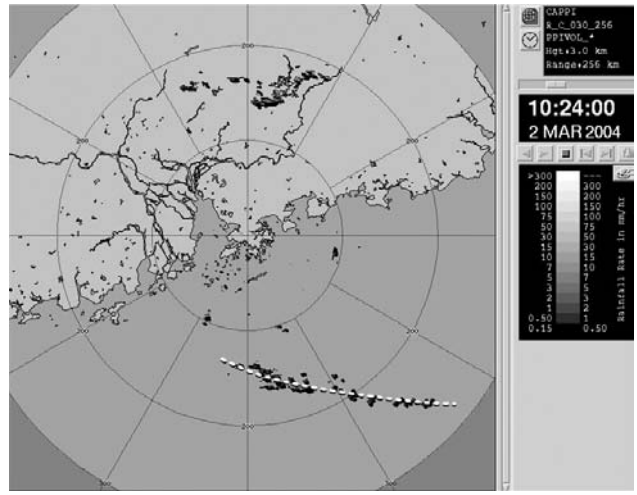

Figure 14. Weather radar image (3 km CAPPI image) of the Hong Kong weather radar on 02 March 2004 at 0224 UTC showing small-scale rain cells arranged along a line (dotted line inserted in the image) whose location corresponds to the location of the wind front visible on the ASAR image depicted in Figure 12 (©HKO).

We note that there is a sharp change in wind speed (marked by different grey scales) and wind direction (marked by arrows) across the front. To the north of the front, northeasterly winds of about 15 ms^{-1} were blowing and to the south, much weaker winds of 2 to 5 ms^{-1} prevailed. This very large difference in wind speed on both sides of the front explains the large difference in backscattered radar power and hence of the image intensity across the frontal line on the ENVISAT ASAR image (Figures 12 and 13). Note that the QUIKSCAT wind map confirms our previous supposition that south of the front the wind speed was so low that hardly any Bragg waves could be generated to cause radar backscattering. This explains why this area looks quite dark on the ASAR image.

The strong change in wind speed and direction across the front was also measured in-situ at the meteorological station on Waglan Island, Hong Kong. If we assume that the wind field relative to the cold front as measured by QUIKSCAT had not changed much on its way south crossing Hong Kong, one would expect that, before the arrival of the cold front, the wind at Waglan Island would have been in the range of 3 to 5 ms^{-1}. The winds then would have strengthened to 15 ms^{-1} from the northeast after passage of the cold front. This was indeed measured on Waglan Island as evidenced by the wind and temperature readings depicted in Figure 17. It can be seen from these readings

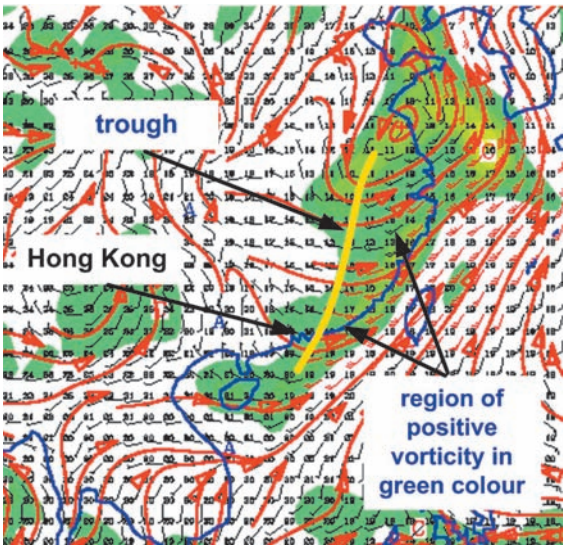

(a)

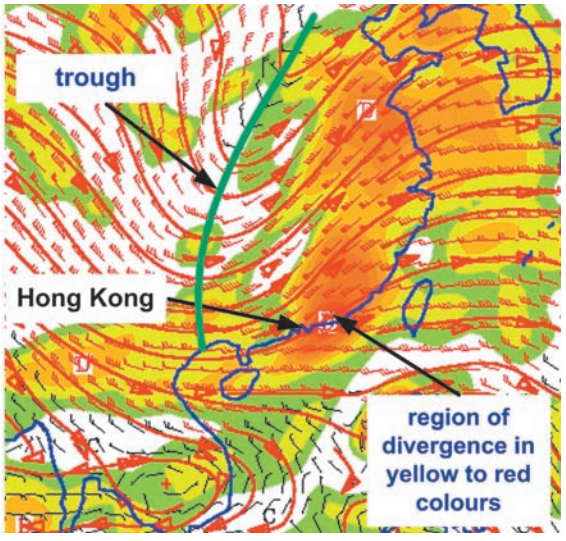

(b)

Plate 2. Wind charts on 08 May 2004 at 0000 UTC (a) at the 850 hPa level, showing a deep trough (the line in yellow color) lying across the southeastern part of China. Streamlines of the wind field are depicted as red lines while regions of positive vorticity are shown in green colours; (b) at the 200 hPa level, showing a trough (the line in dark green color) lying across China. Streamlines of the wind field are depicted as red lines while regions of divergence are shown in yellow to red colors. Coastlines are in blue color.

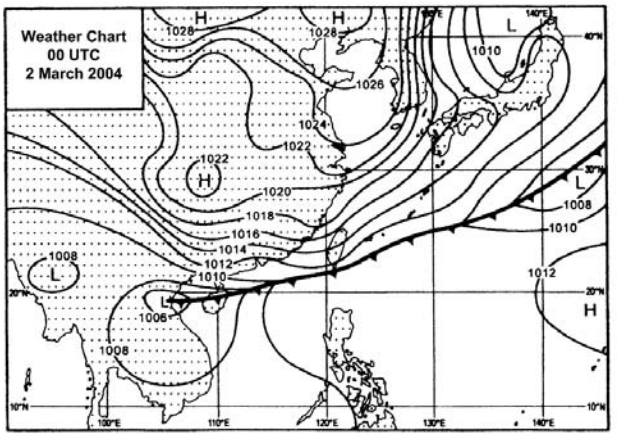

Figure 15. Surface weather map of 02 March 2004 at 0000 UTC showing a cold front over the northern part of the South China Sea.

that winds were generally from the south at about 5 ms^{-1} before the arrival of the cold front which is consistent with the QUIKSCAT wind map. At around 1740 UTC, winds at Waglan Island shifted to the north. This was accompanied by a drop in temperature, which fell from 22°C to 18°C in just three hours. By 2000 UTC, the winds had veered to the northeast and strengthened to 10 ms^{-1}. This is also consistent with the QUIKSCAT wind map, except that the northeasterly winds shown on the QUIKSCAT wind map (Figure 16) are about 5 ms^{-1} stronger than the winds measured at Waglan Island. This can be explained by the difference in surface roughness over land and sea. Since Waglan Island is close to land and since the surface roughness is higher over land than over the open sea, the winds would be stronger over the sea as seen on the QUIKSCAT wind map.

Conclusions

In this paper we have analyzed three rain events over the South China Sea for which synthetic aperture radar images from the Advanced Synthetic Aperture Radar (ASAR) onboard the European satellite ENVISAT are available. On all of these images sea surface manifestations of rain cells are visible. In order to verify that the features are indeed sea surface manifestations of rain cells, we have compared them with quasi-simultaneously acquired weather radar images of the Hong Kong Observatory.

Since the ASAR is a high-resolution imaging instrument, it yields information on the fine-scale structure of rain events that cannot be obtained by other spaceborne instruments designed to measure rain. In the Wide Swath Mode (WSM) the ASAR has a resolution of 150 m, and in the Image Mode (IM) a resolution of 30 m. The instrument with the next best spatial resolution to measure rain from space is the Precipitation Radar (PR) onboard the TRMM satellite which has a resolution of 4 km.

Up to now, no algorithm has been developed to extract rain rates from C-band SAR images. It hardly seems possible to extract them from the intensity of the backscattered radar signals which are scattered from sea areas hit by the raindrops. The reason is that the Bragg waves responsible for the radar backscattering at this radar frequency are affected by the impinging rain drops onto the sea surface in a rather intricate way: they are enhanced (by ring wave generation) as well as attenuated (by turbulence in the upper water layer generated by the impinging rain drops). The calibration function describing the dependence of the backscattered radar on rain rate is very likely a non-monotonic function which also depends on drop size distribution, rainfall history, and wind speed.

However, it is possible to extract the strength of the downdraft from the SAR images by measuring the extent of the downdraft pattern and/or the image intensity of this pattern which is related to wind speed. By measuring the

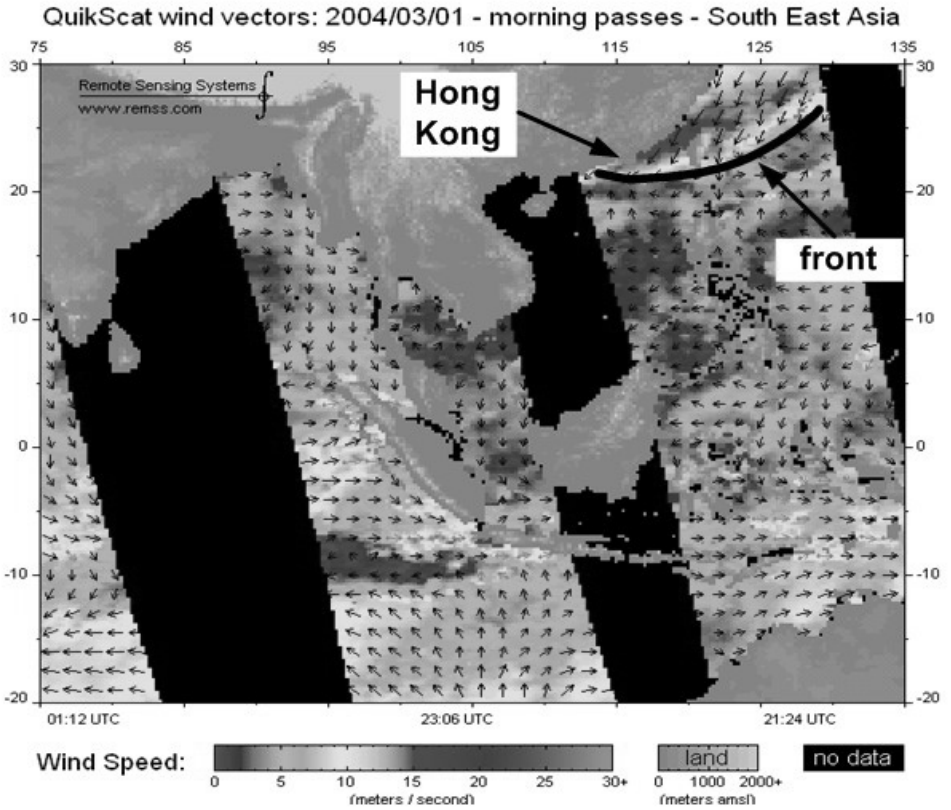

Figure 16. Sea surface wind field map generated from QUIKSCAT data acquired on 01 March 2004 showing a strong wind front over the South China Sea southwest of Hong Kong. The data in that sea area were acquired around 2124 UTC.

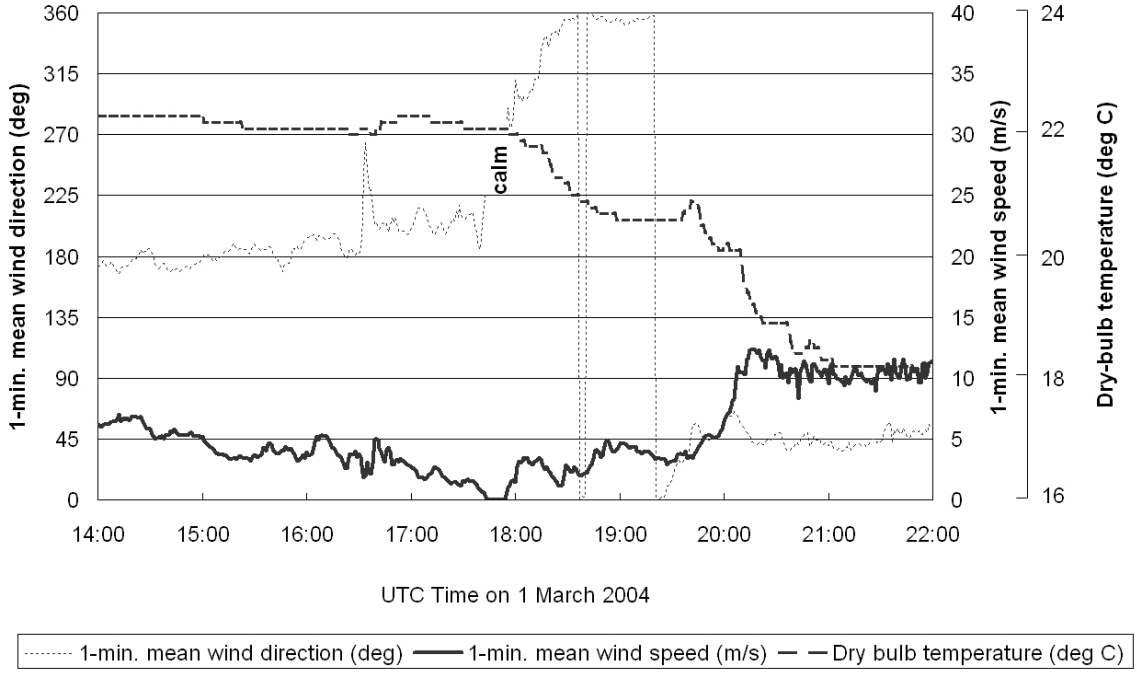

Figure 17. Time series of wind direction, wind speed and dry bulb temperature recorded at Waglan Island, Hong Kong, during the passage of the cold front around 2000 UTC on 01 March 2004, where the wind speed increased from 5 ms^{-1} to 10 ms^{-1}.

downdraft it should be possible to obtain some information on the rain rate.

But even if it were not possible to obtain rain rate information from spaceborne C-band SAR images, these images nevertheless are of great value because they yield information on the distribution of rain cells over the World's ocean on a much finer scale than any other spaceborne rain sensor. In particular, they yield information on the distribution of rain cells along, ahead, and behind atmospheric fronts.

SAR radar signatures of rain events over the ocean can sometimes be confounded with radar signatures originating from other atmospheric phenomena or from oceanic phenomena. By comparing a large number of weather radar images with ENVISAT ASAR images acquired simultaneously over the sea area in reach of the Hong Kong weather radar, one can get a much better understanding of ASAR radar signatures of rain cells. This knowledge can then be used to better interpret ASAR images showing sea surface manifestations of rain cells which have been acquired over sea areas lying out of reach of weather radar stations.

SAR images of rain cells acquired over the ocean are of great value if they are used in combination with other data and with models on the generation of rain cells. The three case studies of rain events presented in this paper illustrate that there is a great potential to study rain cells over the ocean by synergistic use of multi-sensor satellite and ground-based meteorological data.

References

Alpers, W., and C. Melsheimer, 2004. Rainfall, Chapter 17, *Synthetic Aperture Radar Marine User's Manual* (Ch. R. Jackson and J.R. Apel, editors), National Oceanic and Atmospheric Administration, Center for Satellite Application and Research, NOAA/NESDIS, Washington, D.C., pp. 355–371, URL: *http://www.sarusersmanual.com* (last date accessed: 23 January 2007).

Atlas, D., 1994a. Footprints of storms on the sea: A view from spaceborne synthetic aperture radar, *Journal of Geophysical Research*, 99:7961–7969.

Atlas, D., 1994b. Origin of storm footprints on the sea seen by synthetic aperture radar, *Science*, 266:1364–1366.

Bliven, L., P.W. Sobieski, and C. Craeye, 1997. Rain generated ring-waves: Measurements and modelling for remote sensing, *International Journal of Remote Sensing*, 18:221–228.

Craeye, C., P.W. Sobieski, and L.F. Bliven, 1997. Scattering by artificial wind and rain roughened water surfaces at oblique incidences, *International Journal of Remote Sensing*, 18:2241–2246.

Fu, L.-L., and B. Holt, 1982. Seasat views oceans and sea ice with synthetic aperture radar, *JPL Publication 81–120*, 200 p.

Jameson, A.R., F.K. Li, S.L. Durden, Z.S. Haddad, B. Holt, T. Fogarty, E. Im, and R.K. Moore, 1997. SIR-C/X-SAR observations of rain storms, *Remote Sensing of Environment*, 59:267–279.

Kummerow, C., W. Barnes, T. Kozu, J. Shiue, and J. Simpson, 1998. The tropical rainfall measuring mission (TRMM) sensor package, *Journal of Atmospheric and Oceanic Technology*, 15:809–817.

Lin, I.-I., W. Alpers, V. Khoo, H. Lim, T.K. Lim, and D. Kasilingam, 2001. An ERS-1 synthetic aperture radar image of a tropical squall line compared with weather radar data, *IEEE - Transactions on Geoscience and Remote Sensing*, 39(5): 937–945.

Melsheimer, C., W. Alpers, and M. Gade, 1998. Investigation of multi-frequency/multi-polarization radar signatures of rain cells over the ocean using SIR-C/X-SAR data, *Journal of Geophysical Research*, 103:18,867–18,884.

Melsheimer, C., W. Alpers, and M. Gade, 2001. Simultaneous observations of rain cells over the ocean by the synthetic aperture radar onboard the ERS satellites and by surface-based weather radars, *Journal of Geophysical Research*, 106 (C3): 4665–4678.

Moore, R.K., A. Mogili, Y. Fang, B. Beh, and A. Ahamad, 1997. Rain measurement with SIR-C/X-SAR, *Remote Sensing of Environment*, 59:280–293.

Nystuen, J., 1990. A note on the attenuation of surface gravity waves by rainfall, *Journal of Geophysical Research*, 95:18,353–18,355.

Sauvageot, A., 1991. *Radar Meteorology*, Norwood, Massachusetts, Artech House.

Simpson, J., C. Kummerow, W.-K. Tao, and R.F. Adler, 1996. On the Tropical Rainfall Measuring Mission (TRMM), *Meteorology and Atmospheric Physics*, 60:19–36.

Tsimplis, M., 1992. The effect of rain in calming the sea, *Journal of Physical Oceanography*, 22:404–412.

Valenzuela, G.R., 1978. Theories for the interaction of electromagnetic and ocean waves – A review, *Boundary Layer Meteorology*, 13:61–85.